energies

MDPI

Article

Impact of Static Air-Gap Eccentricity Fault on Synchronous Generator Efficiency

Yu-Ling He, Ling Tang, Kai Sun, Wen-Hao Zhang, Xue-Wei Wu and Hai-Peng Wang *

Hebei Key Laboratory of Electric Machinery Maintenance and Failure Prevention, Baoding 071003, China
* Correspondence: wanghpmail@ncepu.edu.cn

Abstract: This paper presents a precise analysis of the efficiency characteristic of the synchronous generator under both normal and SAGE conditions. In this work, various losses of the synchronous generator are computed by the qualitative theoretical model and the finite element analysis in detail. Further, the generator efficiency model is proposed according to the relationship between the output power and the loss. The presented model is verified in a 5-kW non-salient synchronous generator. The result demonstrates that the loss increases and the efficiency reduce as the SAGE intensifies.

Keywords: synchronous generator; static air-gap eccentricity; loss; efficiency; FEA

1. Introduction

Commonly, the generator develops a static air-gap eccentricity (SAGE) fault due to manufacturing error and component wear during operation. The SAGE fault degrades generator performance, or worse, damages the generator. Hence, the SAGE fault should be focused on to prevent the occurrence of adverse consequences during the generator operation.

Currently, the electromechanical generator characteristics with the occurrence of SAGE fault are one of the main research directions. For instance, the electromagnetic forces [1], the electromagnetic torque [2], the unbalanced magnetic pull, and the vibration properties [3–6] are comprehensively studied under the SAGE condition. Besides, Bruzzese C. et al. found that the amplitude of the second harmonic ripple in rotor current is proportional to the degree of the SAGE fault [7], and the first and third harmonic amplitudes of the electromotive force increased significantly under the SAGE fault [8]. Based on the electromechanical characteristics, diagnosis and monitoring of SAGE faults are carried out [9–14]. In addition, the magnetic flux and the shaft voltage are common and useful indicators to measure air-gap eccentricity. Meanwhile, there are also other methods, such as the capacitive and inductive sensors and the Cramer–Rao lower bound technique, to minimize static eccentricity identification error [15]. In addition to the studies related to fault diagnosis and monitoring of the synchronous generator, more and more research on suppression of the SAGE is also being explored [16].

Besides, many scholars have done plenty of detailed research on the loss of the generator. Typically, C. P. Steinmetz devised the Steinmetz equation creatively to compute the core loss [17]. However, applying the calculation formula is relatively inaccurate as some loss is neglected in the calculation process. Therefore, in 1988, Berototti proposed a new method for calculating iron consumption, which has been widely used in this field [18]. Further, some scholars have improved the formula to improve the accuracy of the calculation results [19]. In addition, scholars also focus on the influence of generator structural parameters on the loss and have carried out further research on the temperature rise caused by generator loss [20,21]. In ref. [22], the additional loss and other harmful quantities of an induction motor are estimated comprehensively under SAGE conditions. However, the effect of the SAGE fault on the efficiency of the synchronous generator is not analyzed qualitatively further.

Citation: He, Y.-L.; Tang, L.; Sun, K.; Zhang, W.-H.; Wu, X.-W.; Wang, H.-P. Impact of Static Air-Gap Eccentricity Fault on Synchronous Generator Efficiency. *Energies* **2023**, *16*, 3294. https://doi.org/10.3390/en16073294

Academic Editor: Lorand Szabo

Received: 29 November 2022
Revised: 24 March 2023
Accepted: 3 April 2023
Published: 6 April 2023

Efficiency, as an important parameter to measure generator performance, is closely linked with generator loss. The efficiency estimation based on the power loss mechanism is effective for the efficiency conversion of Marine generators with a low power factor [23]. B. Lu proposed an efficiency evaluation method for in-service motors by calculating air-gap torque [24]. Further, to improve generator efficiency, many scholars have put forward various efficiency optimization methods. For instance, based on the original PNGV Systems Analysis Toolkit program, M. Gokasan designed the sliding mode controller strategy to limit the generator operation within the optimal efficiency region [25]. Mirahki succeeded in increasing starting torque through the combined genetic algorithms and lumped parameter approach [26]. In addition to increasing generator efficiency via the algorithm, there are also many studies on efficiency optimization through improving the structure and configuration of the synchronous generator [27–29]. For example, Grachev achieved efficiency optimization by reducing the volume of wind turbines based on the compact winding structure [30]. To improve the power density, Bonthu proposed a practical method based on neodymium-based magnets [31]. A large number of studies above focus on improving generator efficiency under normal conditions. However, the calculation characteristic of the generator efficiency has not been carried out under common fault conditions.

In this paper, the theoretical expression of generator efficiency is roundly proposed based on the relationship between the total loss and the generator's output power under normal and SAGE conditions. Further, the correctness of the theoretical model is directly proved by the FEA calculation, and a set of fault simulation experiments are performed to demonstrate the theory's availability indirectly. Generally, the study discussed in the paper offers the contributions as follows:

(1) The losses in the generator, including copper loss, core loss, and mechanical loss, are analyzed in detail, and the expressions of all losses are derived. Further, the efficiency model is proposed according to the loss and the output of the synchronous generator;
(2) Unlike previous studies, which mainly focuses on normal condition, this paper not only focuses on various generator loss under the SAGE conditions but also investigates the generator efficiency variation regularities as the SAGE intensifies.

Based on the loss model of the generator, the calculation expressions of each part's loss and operation efficiency are given. Besides, the variations of the loss and efficiency under different SAGE degrees are discussed in detail, which provides a reference for efficiency optimization and reliability enhancement based on the loss model. Additionally, In Section 2, expressions for different types of losses and the theoretical model of efficiency are presented. The FEA calculation is adopted to obtain the detailed loss and the output power of the generator in Section 3. Moreover, in Section 4, the experiment is carried out to verify the efficiency variation of a 5-kW non-salient synchronous generator. In Section 5, the primary conclusion obtained through the work is discussed.

2. Theory Analysis

2.1. The MFD Model

SAGE changes the magnetic field of the generator because the generator's physical parameters vary. The magnetic flux density (MFD), as an important parameter to measure magnetic field performance, can be obtained according to magnetomotive force (MMF) and the permeability per unit area. Generally, the permeability per unit area depends on the air-gap distribution. Hence, the permeability per unit area can be considered a constant under the normal condition due to the circumferential symmetric air-gap. However, no matter how precise the generator is, static eccentricity also exists during operation. As is demonstrated in Figure 1, the generator air-gap distribution changes with the presence of SAGE. θ and α_m represent the direction of the rotor displacement and the mechanical angle characterizing the circumferential position, respectively. Besides, the air-gap length is a constant g_0 under normal conditions.

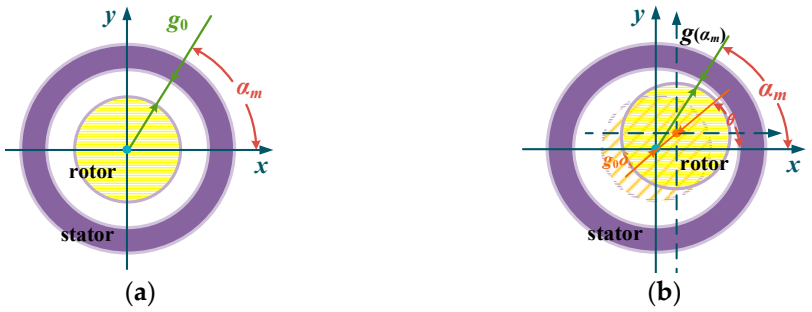

Figure 1. Distribution diagram of generator air-gap: (**a**) Normal condition; (**b**) SAGE condition.

Based on Figure 1 and geometry theory, the air-gap length $g(\alpha_m)$ can be obtained.

$$g(\alpha_m) = \begin{cases} g_0 & \text{Normal} \\ g_0(1 - \delta_s \cos(\alpha_m - \theta)) & \text{SAGE} \end{cases} \tag{1}$$

where δ_s is positively correlated with the degree of eccentricity.

Considering the relationship between reluctance and permeability, the permeance per unit area can be expanded by the Maclaurin series based on the air permeability μ_0:

$$\Lambda(\alpha_m) = \frac{\mu_0}{g(\alpha_m)} = \begin{cases} \mu_0/g_0 = \Lambda_0 & \text{Normal} \\ \Lambda_0(1 + \delta_s \cos(\alpha_m - \theta) + \delta_s^2 \cos^2(\alpha_m - \theta) + \cdot\cdot) & \text{SAGE} \end{cases} \tag{2}$$

where Λ_0 represents the magnetic permeance per unit area under normal conditions.

According to Figure 2, the fundamental MMF is made of the MMF F_s of the armature winding and the MMF F_r of the field winding based on the vector superposition law. The SAGE fault does not change the generator circuit. Hence, compared to the MMF under normal conditions, the MMF under the SAGE conditions is the same and is described by (3).

$$\begin{aligned} f(\alpha_m, t) &= F_r \cos(\omega t - \alpha_m + 0.5\pi + \psi) + F_s \cos(\omega t - \alpha_m) \\ &= F_c \cos(\omega t - \alpha_m - \beta) \end{aligned} \tag{3}$$

where:

$$\begin{cases} F = \sqrt{(F_r - F_s \sin\psi)^2 + (F_s \cos\psi)^2} \\ \beta = \arctan\frac{F_s \cos\psi}{F_r - F_s \sin\psi} \end{cases} \tag{4}$$

where ω and ψ are the electrical angular frequency and the internal power angle, respectively. F is the synthetic MMF, I denotes armature current, and E_0 is the generator electromotive force without load.

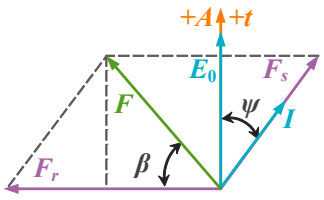

Figure 2. Fundamental MMF of synchronous generator.

Therefore, ignoring the high-order components that exist in the expansion item, the MFD expression is derived as follows:

$$\begin{cases} B_n(\alpha_m,t) &= F\Lambda_0\cos(\omega t-\alpha_m-\beta) & \text{Normal}\\ B_e(\alpha_m,t) &= F\Lambda_0\cos(\omega t-\alpha_m-\beta)\times(1+\delta_s\cos(\alpha_m-\theta)+0.5\delta_s^2+0.5\delta_s^2\cos 2(\alpha_m-\theta)) & \\ &= 0.5\,F\Lambda_0\delta_s\cos(\omega t-\theta-\beta)+ & \\ &\sqrt{1+\delta_s^2+0.5\delta_s^2\cos(2(\alpha_m+\theta))}\,F\Lambda_0\cos(\omega t+\alpha_m-2\theta-\beta+\theta_1)+ & \\ &0.5\,F\Lambda_0\delta_s\cos(\omega t-2\alpha_m+\theta-\beta)+0.25F\Lambda_0\delta_s^2\cos(\omega t-3\alpha_m+2\theta-\beta) & \text{SAGE}\\ &\theta_1=\arccos\frac{\cos 2(\alpha_m+\theta)}{\sqrt{1+\delta_s^2+0.5\delta_s^2\cos(2(\alpha_m+\theta))}} & \end{cases} \tag{5}$$

According to (5), the MFD is a time-space function due to the parameter t and the parameter α_m. Both time harmonics and space harmonics are the fundamental frequency under normal conditions. Observing the MFD under the SAGE condition, the time harmonic component in the MFD is still the fundamental frequency. The thing to notice is the amplitude of the fundamental which rest with the spatial position. Compared with the amplitude under normal conditions, the fundamental amplitude increases if α_{m} satisfies $|\alpha_m-\theta|\le 0.5\pi$; otherwise, the amplitude decrease when the SAGE occurs. Additionally, the MFD frequency spectrum contains the DC component, 1st, 2nd, and 3rd space harmonics by observing α_m in the second equation of (5). The amplitudes of all space frequency components increase as the SAGE intensifies.

2.2. Phase Current Model

The rotation of the magnetic field induces phase current in the armature winding. The expression of the phase current can be obtained in the light of Faraday's law of electromagnetic induction and Ohm's law. The phase current induced in the armature winding at the rotor speed n_r, the stator winding length l, and the angle between two slots α_1 are obtained as follows:

$$\begin{cases} i_n &= qw_ck_wB_n(\alpha_m,t)lv/Z=qw_ck_wB_n(\alpha_m,t)l\pi R_sn_r/30Z & \\ &= qw_ck_wl\pi R_sn_rF\cos(\omega t-\alpha_m-\beta)\frac{\Lambda_0}{30Z} & \text{Normal}\\ i_e &= qw_ck_wB_e(\alpha_m,t)lv/Z=qw_ck_wB_e(\alpha_m,t)l\pi R_sn_r/30Z & \\ &= qw_ck_wl\pi R_sn_rF\cos(\omega t-\alpha_m-\beta)\frac{\Lambda_0}{30Z} & \\ &\times\left(1+\delta_s\cos(\alpha_m-\theta)+0.5\delta_s^2+0.5\delta_s^2\cos 2(\alpha_m-\theta)\right) & \text{SAGE}\\ k_w &= k_{yy}\times k_{q\eta}=\sin\left(90^\circ\times y/\tau\right)\times\sin(q\alpha_1/2)/(q\sin(\alpha_1/2)) & \end{cases} \tag{6}$$

where R_s is the stator core's inner diameter. Q and ω_c are the slots number at each pole in each phase and the turns number in each winding, respectively. $K_{\omega\gamma}$, $k_{yy,}$ and $k_{q\eta}$ are the winding factor, the pitch factor, and the distribution factor, respectively. Z denotes the reactance in the stator winding circuit.

It is observed in (6) that the phase current mounts as the SAGE takes place.

2.3. Generator Loss Model

The loss model of the synchronous generator is established, and the power flow is exhibited obviously in Figure 3. The generator input power consists of the generator's loss and the output power. Further, the loss can be split up into mechanical loss, core loss, and copper loss generated by the joule effect. The parts that need specific attention are the core loss and copper loss. The core loss includes the rotor core loss and the stator core loss, while the copper loss refers to the stator winding copper loss excluding the rotor winding copper loss because the excited current is supplied by the exciter. What's more, both the friction and windage loss are considered.

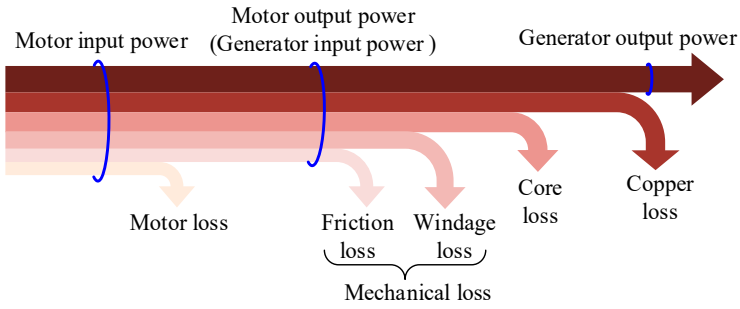

Figure 3. Power flow.

2.3.1. Core Loss

In this paper, the common and valid Bertotti's core loss model is used to calculate the core loss. Generally, the core loss, which includes hysteresis loss P_H, eddy current loss P_C, and excess loss P_E can be expressed by (7).

$$PFe = P_H + P_C + P_E = k_h B_m^2 f + k_c B_m^2 f^2 + k_e B_m^{1.5} f^{1.5} \tag{7}$$

According to (5) and (7), the core loss in the magnetic field with alternating frequency f can be obtained as follows:

$$P_{Fe}(t) = \begin{cases} \left[f\Lambda_0^2 F^2 \cos^2(\omega t - \alpha_m - \beta)\right](k_h + k_c f) & \\ \quad + k_e f^{1.5} \Lambda_0^{1.5} F^{1.5} \cos^{1.5}(\omega t - \alpha_m - \beta) & \text{Normal} \\ (1 + 2\delta_s \cos\alpha_m)\left[f\Lambda_0^2 F^2 \cos^2(\omega t - \alpha_m - \beta)\right](k_h + k_c f) & \\ \quad + (1 + \delta_s \cos\alpha_m)^{1.5} k_e f^{1.5} \Lambda_0^{1.5} F^{1.5} \cos^{1.5}(\omega t - \alpha_m - \beta) & \text{SAGE} \end{cases} \tag{8}$$

where k_h denotes the factor which is relevant to hysteresis loss, k_c is the factor that is relevant to eddy current loss, and k_e is the factor relevant to excess loss. We can see that the core loss is closely related to MFD, and it is positively related to the degree of SAGE.

2.3.2. Stator Copper Loss

The copper loss in stator winding is caused by the thermal effect of electric current. When the generator runs stably, the higher-order harmonic amplitudes of the phase current in the frequency spectrum appear tiny. Hence, in this work, the skin effect and the proximity effect cannot be considered. According to Joule's law, we can derive the stator copper loss as the following equation:

$$P_{Cu} = 3\sum_{\gamma=1}^{N} I_{pm\gamma}^2 R_p \tag{9}$$

Based on (6), the formula of stator core loss can be obtained as follows [32]:

$$\begin{cases} P_{nCu} = q^2 w_c^2 l^2 \pi^2 R_s{}^2 n_r{}^2 R_p \frac{\mu_0^2}{600 g^2 Z^2} k_w^2 F^2 & \text{Normal} \\ P_{eCu} = q^2 w_c^2 l^2 \pi^2 R_s{}^2 n_r{}^2 R_p (1 + 2\delta_s \cos(\alpha_m - \theta)) \frac{\mu_0^2}{600 g^2 Z^2} k_w^2 F^2 & \text{SAGE} \end{cases} \tag{10}$$

Generally, q, w, l, R_S, n_r, and R_p in the formula are all constant in (10) in a generator. The copper loss has a relation to δ_s under the SAGE condition. As the eccentric degree intensifies, the copper loss increases. Moreover, since R_p is generally a constant, the copper loss has the same trend as the phase current, increasing as the SAGE occurs.

2.3.3. Mechanical Loss

Generator mechanical loss mainly comes from friction and wind resistance. The friction loss and the windage loss are expressed approximately by [33,34]:

$$P_{fr} = k_{fb} m_r n_r 10^{-3} \tag{11}$$

$$P_{wind} = 2 D_{ro}^3 l_a n_r^3 10^{-6} \tag{12}$$

where D_{ro} and l_a denote the diameter and the length of the rotor core. K_{fb} is the coefficient acquired by a lot of experience, and m_r is the rotor mass. Since the parameters in the expression of mechanical loss are usually constant, the mechanical loss, which is the sum of the two, also remains constant.

2.4. The Efficiency Model

The input power of the generator can be calculated by [35]:

$$P_{out} = \sqrt{3} U I \cos \varphi \tag{13}$$

where U is the line voltage, I is the line current, and φ is the generator power factor.

Hence, the efficiency η can be obtained as follows:

$$\eta = \frac{P_{out}}{P_{in}} = \frac{\sqrt{3} U I \cos \varphi}{P_{out} + P_{Fe} + P_{Cu} + P_{fr} + P_{wind}} \tag{14}$$

3. FEA Verification

3.1. FEA Setup

As shown in Figure 4a, the universal three-dimensional FEA model of a synchronous generator is set up. The electromechanical parameters of the FEA model are given in Table 1. There is no difference in the external circuit model of both the stator winding and the field winding under normal and SAGE conditions (see Figure 4b). Both the output power and all loss are calculated by the FEA model.

To meet the rated voltage, we set the excitation current to 7.9A and the generator speed to 3000 rpm. Besides, five periods are simulated in FEA, and the step size of the finite element simulation is set as 0.2 ms.

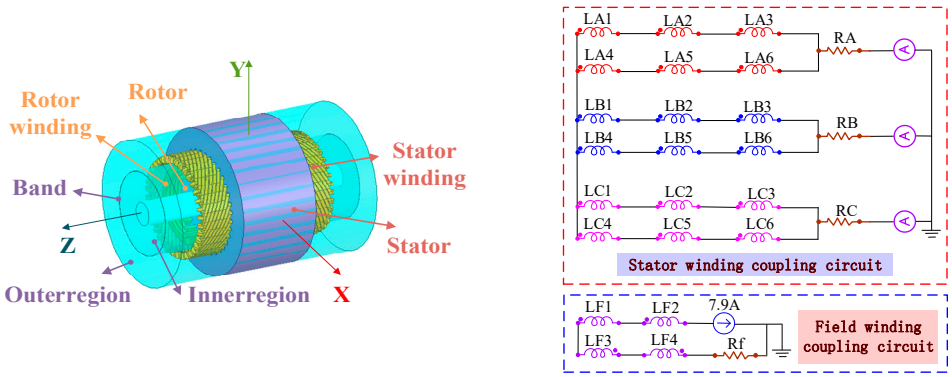

(**a**) (**b**)

Figure 4. FEA simulation: (**a**) simulation model; (**b**) circuit model.

In the process of the FEA simulation, the rotor core and the filed winding in the FE model of the synchronous generator are moved exactly the same distance in the same direction to simulate the SAGE fault. Besides, it is important to note that the center line of rotor rotation is performed exactly the same way. The offset indicates the degree of eccentricity. In this paper, in addition to the finite element simulation under normal conditions, FE calculations under 10%, 20%, and 30% SAGE conditions are also performed.

Table 1. Generator key parameters.

Parameters	Values	Parameters	Values
rated power	5 kVA	stator core length	130 mm
rated excitation current	7.9 A	stator coil turns per slot	22
pole-pairs	1	rotor virtual slots	24
rated power factor	0.8	rotor actual slots	16
air-gap length	1.2 mm	rotor outer diameter	142.6 mm
stator slots	36	rotor inner diameter	40 mm
stator outer diameter	250.5 mm	rotor coil turns per slot	60
stator inner diameter	145 mm	internal power factor	0.62

3.2. FEA Results

3.2.1. MFD Results

Figure 5 shows the curves and the spatial frequency component of the MFD under the normal and the SAGE condition obtained by FEA at 0.06 s. Additionally, a pair of large teethes of the generator rotor are located where the air-gap is the largest, and the air-gap is the smallest at 0.06 s.

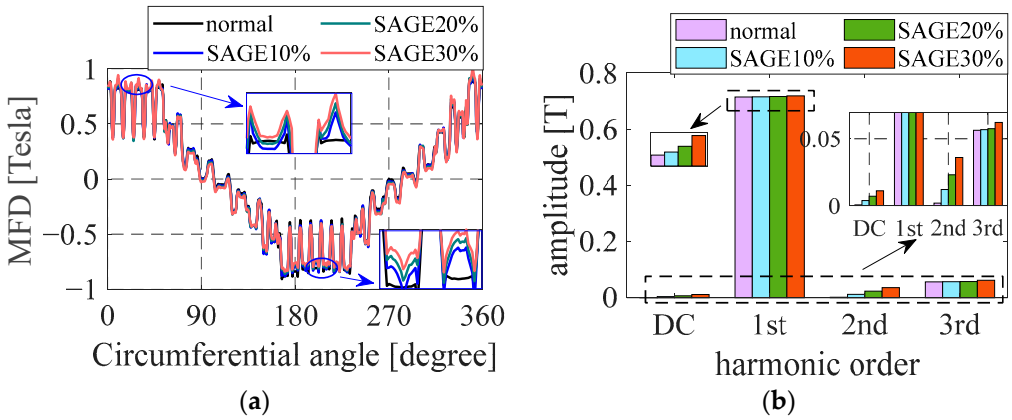

Figure 5. MFD results with different eccentricity: (**a**) MFD curves; (**b**) frequency spectrum.

The circumferential angle where the perks and the troughs of the MFD curves are located is consistent with the spatial position of the rotor big teeth due to the magnetic field distribution. Observing the curves under different SAGE degrees, the MFD results have shifted significantly upward. The main reason for the phenomenon is that the DC component makes the MFD distribution uneven in space. The amplitude of the MFD increases on the side with a smaller air-gap and decreases on the side with a larger air-gap.

Further, to explore the MFD characteristics more clearly, the spectrum is generated based on the MFD curves. Theoretically, only the odd space harmonics occur in the MFD under normal conditions. However, weak DC components and inconspicuous 2nd harmonics are found in the MFD due to the error of the electromagnetic calculation and the discrete Fourier transform under normal conditions. Meanwhile, the DC component amplitude and the harmonic amplitude of MFD significantly augment as the SAGE occurs. The amplitudes increase with the intensification of the eccentricity. Observing αm in (8), the DC component, the fundamental frequency, the 2nd harmonic, and the 3rd harmonic obviously exist under the SAGE condition. The component amplitude is positively correlated with the eccentricity degree. Hence, the result of the FEA calculation is consistent with the theoretical analysis in (8) according to the above analysis.

3.2.2. Current Results

As illustrated in Figure 6, the phase current results are obtained from the FEA calculation under different degrees of SAGE. Compared with the phase current in the normal

condition, the curves of the phase current shift upward just like the MFD curve. And the higher the degree of the eccentricity, the more the amplitude increases. Correspondingly, the phase current RMS increases as the SAGE occurs, as shown in Figure 7. This is well in line with the conclusions of the qualitative analysis above.

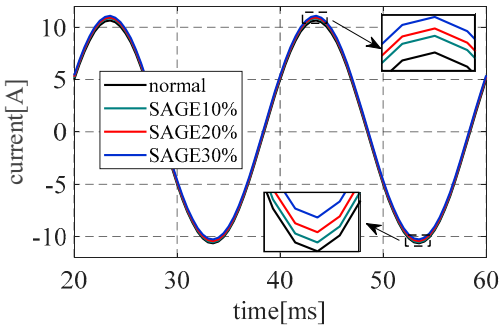

Figure 6. Phase current curves by FEA under normal and SAGE.

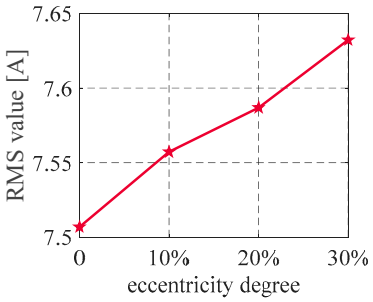

Figure 7. RMS value of phase current by FEA.

3.2.3. Loss Results

As shown in Figure 8, all losses obtained from the FEA with different eccentric degrees are listed. Comparing different kinds of generator losses, the copper loss, as the largest proportion, accounts for about 60 percent of the total loss, followed by the core loss of the stator. The mechanical loss is the minimum among the losses. Furthermore, the copper core loss, the stator core loss, and the total loss increase as the SAGE takes place while the mechanical loss, which depends on the generator structure and the rotation speed, is constant. In particular, it should be noted that the copper loss of the rotor should not be analyzed in the simulation process because the rotor windings are fed through the separate power supply in a synchronous generator. According to (8) and (10), the SAGE causes an increase in the copper loss and the core loss in the generator. Hence, the variation trend of FEA data is consistent with the conclusion of the theoretical model.

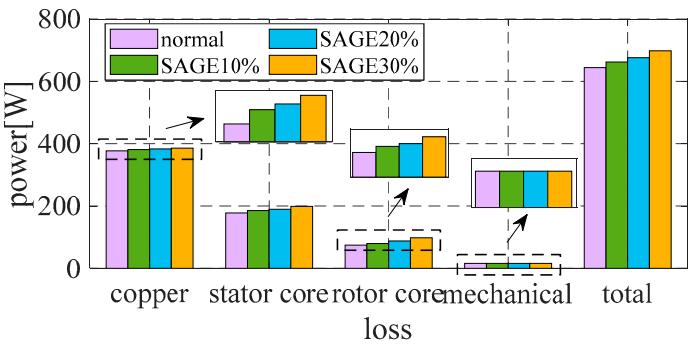

Figure 8. Generator loss by FEA.

3.2.4. Efficiency Results

The generator's output is indicated in Figure 9. The output power curves fluctuate with the harmonics of the phase voltage. Further, the output power increase significantly when the SAGE takes place. The RES value of the generator's output power increases, as shown in Figure 10. Compared with the output under normal conditions, the generator output increases by 17 W under SAGE 10% and increases by 41 W under SAGE 30%.

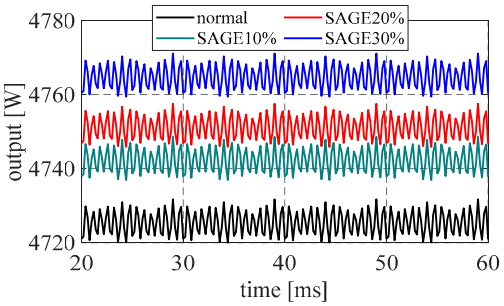

Figure 9. Generator output power by FEA.

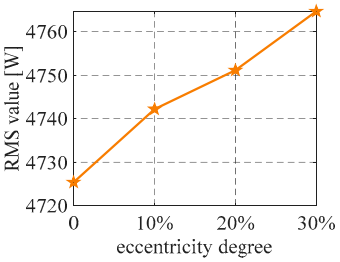

Figure 10. RMS value of output power by FEA.

Further, based on (14), the generator's efficiency can be calculated with precision. The result of the efficiency is shown in Figure 11. It is clear that the efficiency decreases with the increase of the SAGE degree based on the FEA result. Compared with the efficiency under normal conditions, the generator efficiency decreases by 0.9% under SAGE 30%. Although the increase in the output power of the generator is beneficial, the loss increases, and hence, the efficiency of the generator decreases. The result shows that the occurrence of SAGE has a negative effect on the generator performance.

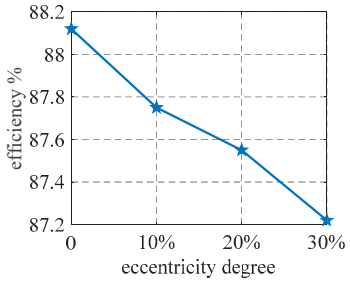

Figure 11. Generator efficiency of FEA.

4. Experimental Verification

4.1. Experimental Setup

Further, experiments are performed to indirectly verify theoretical analyses and simulation calculations. The CS-5 prototype generator is manufactured based on Table 1. As shown in Figure 12, the prototype is driven by a drive motor. The input current of the drive motor is obtained via the current transformer. Meanwhile, the output of the prototype generator is measured by the data collector. To calculate the loss and the efficiency of the

prototype machine accurately in the experiment, the input power to the prototype needs to be measured. However, it is hard to obtain the input torque by adding a torque sensor due to the narrow space between the prototype machine and the drive motor. Hence, we measure the input power of the drive motor and calculate the output power of the drive motor by the efficiency and power factor.

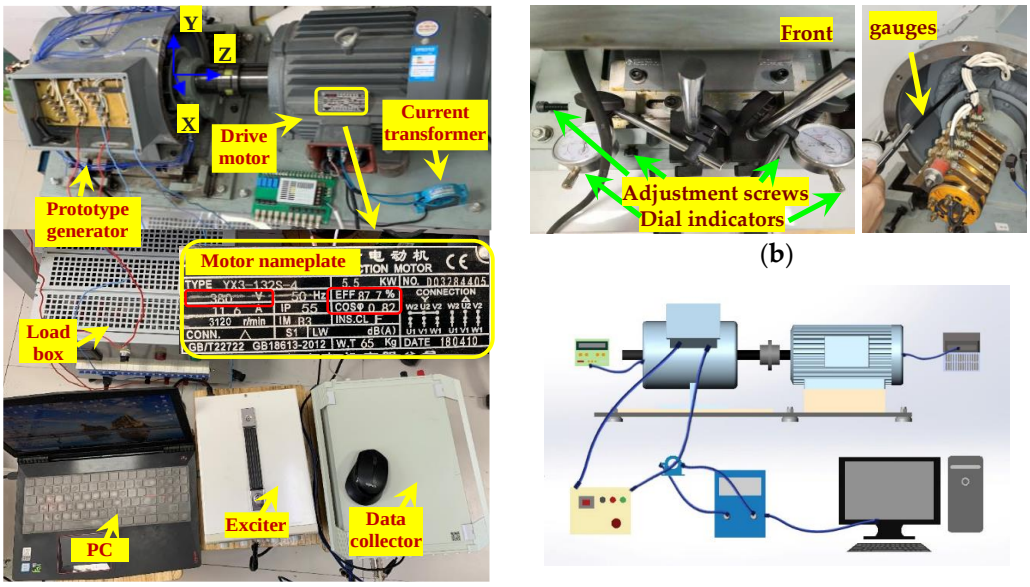

Figure 12. Experiment platform: (**a**) Diagram of equipment; (**b**) SAGE realization; (**c**) Schematic diagram.

Additionally, the rotor is stationary on the test bench, whereas the stator can move relative to the rotor in both horizontal (along X axis) directions via screws, and two dial indicators are used to sense the movement value, as shown in Figure 12b. Thus, the SAGE condition can be simulated by moving the stator core horizontally. The eccentric degree depends on the movement distance. Moreover, the feeler gauge is used to test the accuracy of the air-gap adjustment. In this paper, four sets of experiments were conducted, consistent with the simulation conditions under normal conditions, being 10% SAGE, 20% SAGE, and 30% SAGE, respectively.

4.2. Experimental Results

4.2.1. Measurement of Phase Current

The phase current is measured in the experiments under different SAGE degrees, and the date of the phase current is indicated in Figure 13. Observing the peaks and troughs of the current curves, the wave crest of the phase current increases and the trough value decrease as the SAGE intensifies. The phenomenon is consistent with the result which is obtained by FEA calculation.

In Figure 14a, the RMS value variation of the phase current in the experiments is indicated with different eccentricity degrees. In addition, for clarity, the RMS increase of the phase current is compared between the experiment and the FEA calculation in Figure 14b. It is clear that the RMS value of the phase current increases with the increase of the SAGE degree. The FEA calculation coincides well with the experimental data.

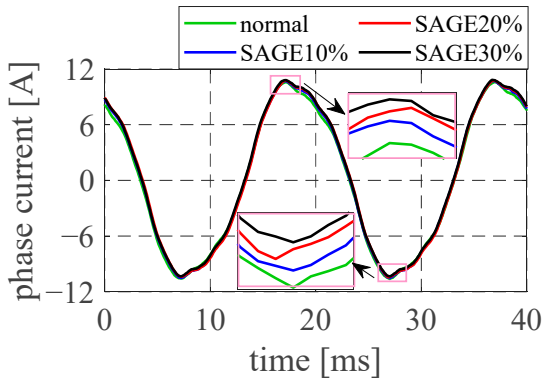

Figure 13. Phase current in experiments.

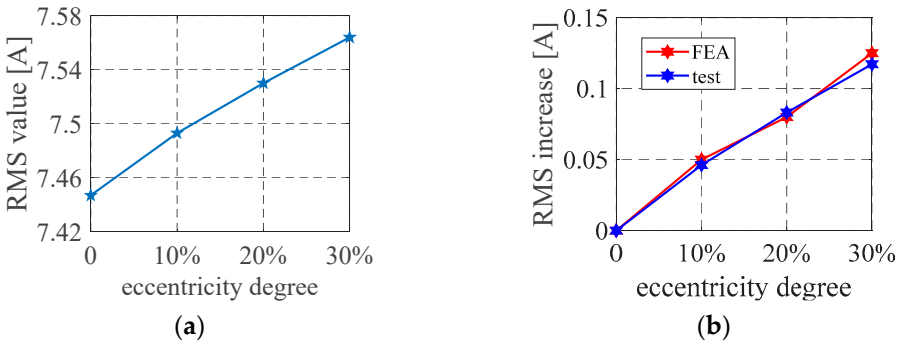

Figure 14. Phase current: (**a**) RMS value of phase current; (**b**) RMS comparison.

4.2.2. Loss Results

As shown in Figure 15, the generator output is obtained in the experiments under different eccentric degrees. For clarity, the corresponding RMS value is indicated in Figure 16. Further, the RMS value increase of the output power in the experiments is compared with that in the FEA calculation, as shown in Figure 16b. The result shows that the output increases due to the increase of the phase current as the SAGE takes place, and the RMS increase obtained by different methods is roughly the same.

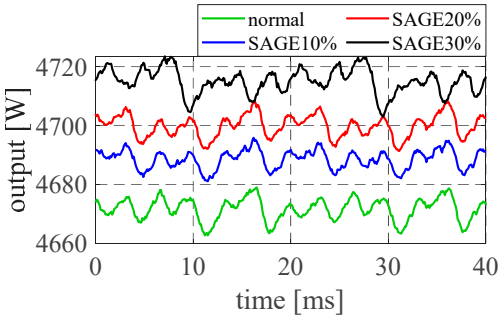

Figure 15. Output in experiments.

To obtain the generator input, the output of the drive motor Pm-out is calculated based on motor power factor φ_{m} and motor efficiency η_{m}.

$$P_{m-out} = \sqrt{3} U_m I_m \cos \varphi_m \eta_m \tag{15}$$

where U_{m} and I_{m} represents the line phase and the line current, respectively.

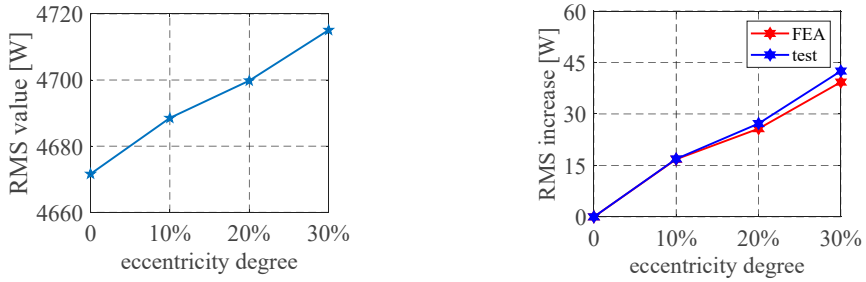

Figure 16. Output: (**a**) RMS value of output; (**b**) RMS output increase.

The line current of the motor under the normal and the SAGE condition is indicated in Figure 17. Observing the input current curves, the amplitude of the line current increases significantly when the SAGE occurs. And the greater the eccentric degree, the higher the amplitude.

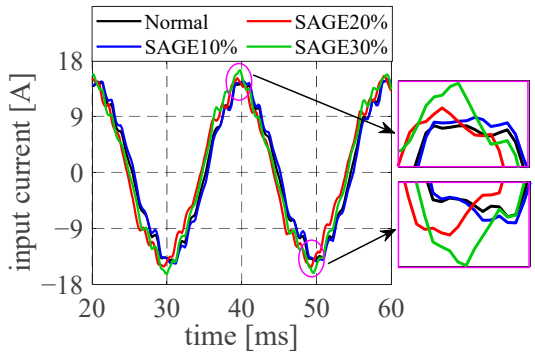

Figure 17. Motor input current.

Unlike the total loss, which is obtained by multiplying various losses in FEA calculations, the total loss in the experiment is obtained by subtracting the output power from the generator input power. Hence, the loss P_{loss} of the generator can be calculated by the following:

$$P_{loss} = P_{in} - P_{out} = P_{m-out} - P_{out} \tag{16}$$

The data on the total loss can be obtained in Figure 18. The 644 W loss power is generated in the generator under normal conditions. The loss of power increases as the SAGE intensifies. Compared with the loss under the normal condition, the loss power under 30% eccentric degree condition increases by about 60 W. Additionally, Figure 18b shows that the experimental results align with the simulation calculation.

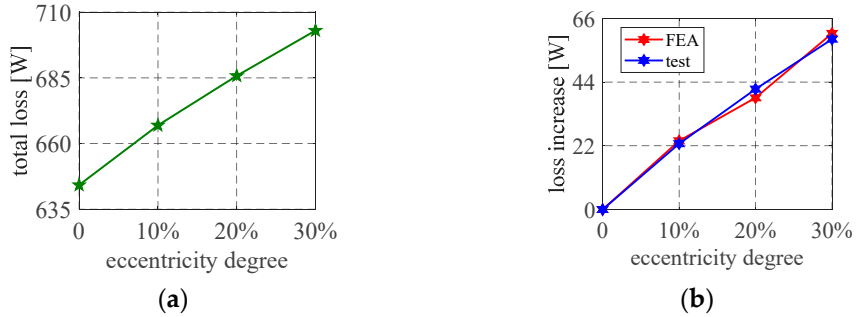

Figure 18. Motor input current: (**a**) Total loss by experiment; (**b**) Loss increase under different eccentric degrees.

4.2.3. Efficiency Results

Based on (14), the generator efficiency can be computed as follows:

$$\eta = \frac{P_{out}}{P_{in}} = \frac{P_{out}}{P_{m-out}} \tag{17}$$

The efficiency result obtained by the experiments is illustrated in Figure 19. The result shows that the generator efficiency significantly decreases with the occurrence of the SAGE. Although the generator output increases, the effect of the loss increase on the generator efficiency is stronger than that of the output increase. The generator efficiency decreases as the SAGE intensifies. Comparing Figure 19a with Figure 11, the generator efficiency of the FEA calculation is generally more than that obtained by the experiments due to the leakage magnetic field and the installation error. However, the change in trend and the variation of the generator efficiency obtained by the FEA calculation and the experiments remain the same under different eccentric degrees.

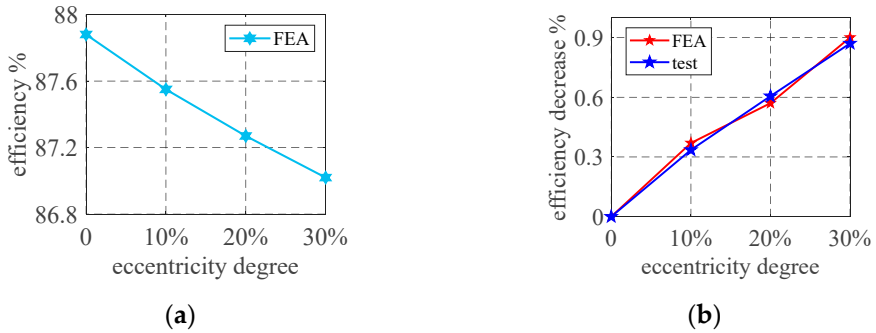

Figure 19. Generator efficiency under different eccentric degrees: (**a**) Variation; (**b**) Decrease.

5. Conclusions

The efficiency model of the synchronous generator is proposed in detail, and the impact of the SAGE on the generator efficiency is discussed comprehensively in this paper. The efficiency is computed via theoretical analysis according to the power flow of the generator. The expressions of the loss and the efficiency under the SAGE condition are derived. Further, the FEA calculation is adopted to obtain the loss and the output of the generator under the normal and the SAGE condition. Finally, experiments are carried out on a prototype generator to confirm the calculation strictly. The result shows that the total loss and the output power of the generator increase while the generator efficiency generally decreases with the increase of the SAGE degree. The SAGE fault has a significant hazard to the generator efficiency. The generator should be monitored to prevent the SAGE fault, which reduces the generator's performance.

Author Contributions: Conceptualization, Y.-L.H. and L.T.; methodology, K.S.; software, W.-H.Z.; validation, X.-W.W., H.-P.W. and Y.-L.H.; formal analysis, L.T.; data curation, Y.-L.H.; writing—original draft preparation, L.T.; writing—review and editing, K.S.; visualization, H.-P.W.; supervision, H.-P.W.; project administration, Y.-L.H.; funding acquisition, Y.-L.H. All authors have read and agreed to the published version of the manuscript.

Funding: This research was supported in part by the National Natural Science Foundation of China (52177042), the Hebei Provincial Natural Science Foundation (E2020502032), the Chinese Fundamental Research Funds for the Central Universities (2018YQ03), and the 3rd Top Youth Talent Support Program of Hebei Province ([2018]-27).

Data Availability Statement: Not applicable.

Conflicts of Interest: The authors declare no conflict of interest.

References

1. Dirani, H.C.; Merkhouf, A.; Giroux, A.M.; Kedjar, B.; Al-Haddad, K. Impact of Real Air-Gap Nonuniformity on the Electromagnetic Forces of a Large Hydro-Generator. *IEEE Trans. Ind. Electron.* **2018**, *65*, 8464–8475. [CrossRef]
2. He, Y.L.; Xu, M.X.; Xiong, J.; Sun, Y.X.; Wang, X.L.; Gerada, D.; Vakil, G. Effect of 3D Unidirectional and Hybrid SAGE on Electromagnetic Torque Fluctuation Characteristics in Synchronous Generator. *IEEE Access* **2019**, *7*, 100813–100823. [CrossRef]
3. Khajueezadeh, M.S.; FeizHoseini, S.; Nasiri-Gheidari, Z.; Behzad, M. Analysis of Torsional Vibrations on the Resolver Under Eccentricity in PMSM Drive System. *IEEE Sens. J.* **2022**, *22*, 21592–21599. [CrossRef]
4. Echeverria, J.J.R.; da Silva, P.V.V.; da Costa Bortoni, E. Analysis of Orbital Eccentricity and UMP in Large Salient Pole Synchronous Machines. *IEEE Trans. Ind. Appl.* **2019**, *55*, 4715–4722. [CrossRef]
5. He, Y.L.; Zhang, Y.Y.; Xu, M.X.; Wang, X.L.; Xiong, J. New Hybrid Model for Electromechanical Characteristic Analysis Under SISC in Synchronous Generators. *IEEE Trans. Ind. Electron.* **2020**, *67*, 2348–2359. [CrossRef]
6. He, Y.L.; Sun, Y.X.; Xu, M.X.; Wang, X.L.; Wu, Y.C.; Vakil, G.; Gerada, D.; Gerada, C. Rotor UMP Characteristics and Vibration Properties in Synchronous Generator Due to 3D Static Air-Gap Eccentricity Faults. *IET Electr. Power Appl.* **2020**, *14*, 961–971. [CrossRef]
7. Bruzzese, C.; Joksimovic, G.; Santini, E. Static Eccentricity Detection in Synchronous Generators by Field Current and Stator Voltage Signature Analysis—Part II: Measurements. In Proceedings of the XIX International Conference on Electrical Machines—ICEM 2010, Rome, Italy, 6–8 September 2010; pp. 1–5.
8. Bruzzese, C.; Giordani, A.; Santini, E. Static and Dynamic Rotor Eccentricity On-Line Detection and Discrimination in Synchronous Generators by No-Load E.M.F. Space Vector Loci Analysis. In Proceedings of the 2008 International Symposium on Power Electronics, Electrical Drives, Automation and Motion, Ischia, Italy, 11–13 June 2008; pp. 1259–1264.
9. Zhu, Z.Q.; Wu, L.J.; Jamil, M.L.M. Distortion of Back-EMF and Torque of PM Brushless Machines Due to Eccentricity. *IEEE Trans. Magn.* **2013**, *49*, 4927–4936. [CrossRef]
10. Ma, C.; Li, J.; Zhang, N.; Bu, F.; Yang, Z. Open-Circuit Radial Stray Magnetic Flux Density Based Noninvasive Diagnosis for Mixed Eccentricity Parameters of Interior Permanent Magnet Synchronous Motors in Electric Vehicles. *IEEE Trans. Ind. Electron.* **2023**, *70*, 1983–1992. [CrossRef]
11. He, Y.L.; Zhang, Z.J.; Tao, W.Q.; Wang, X.L.; Gerada, D.; Gerada, C.; Gao, P. A New External Search Coil Based Method to Detect Detailed Static Air-Gap Eccentricity Position in Nonsalient Pole Synchronous Generators. *IEEE Trans. Ind. Electron.* **2021**, *68*, 7535–7544. [CrossRef]
12. Caetano, R.E.; Chabu, I.E.; Stolfi, G.; Santos, J.C.; Nagao, S.; Gomes, C.E.; Paiva, R.D.; Nabeta, S.I.; Micerino, F.J. Capacitive and Inductive Sensors for Diagnosing Air-Gap Anomalies in Synchronous Generators. In Proceedings of the 2015 IEEE International Electric Machines & Drives Conference (IEMDC), Coeur d'Alene, ID, USA, 10–13 May 2015; pp. 637–641.
13. Wu, X.; Zhu, Z.Q.; Wu, Z.Y.; Liu, T.Y.; Li, Y.X. Analysis and Suppression of Rotor Eccentricity Effects on Fundamental Model Based Sensorless Control of Permanent Magnet Synchronous Machine. *IEEE Trans. Ind. Appl.* **2020**, *56*, 4896–4905. [CrossRef]
14. Mirzaeva, G.; Saad, K.I. Advanced Diagnosis of Rotor Faults and Eccentricity in Induction Motors Based on Internal Flux Measurement. *IEEE Trans. Ind. Appl.* **2018**, *54*, 2981–2991. [CrossRef]
15. Doorsamy, W.; Abdallh, A.A.; Cronje, W.A.; Dupré, L. An Experimental Design for Static Eccentricity Detection in Synchronous Machines Using a Cramér–Rao Lower Bound Technique. *IEEE Trans. Energy Convers.* **2015**, *30*, 254–261. [CrossRef]
16. Nasiri-Gheidari, Z.; Tootoonchian, F. Axial Flux Resolver Design Techniques for Minimizing Position Error Due to Static Eccentricities. *IEEE Sens. J.* **2015**, *15*, 4027–4034. [CrossRef]
17. Steinmetz, C.P. On the Law of Hysteresis. *Trans. Am. Inst. Electr. Eng.* **1892**, *9*, 1–64. [CrossRef]
18. Bertotti, G. General Properties of Power Losses in Soft Ferromagnetic Materials. *IEEE Trans. Magn.* **1988**, *24*, 621–630. [CrossRef]
19. Kim, C.W.; Kim, J.M.; Seo, S.W.; Ahn, J.H.; Hong, K.; Choi, J.Y. Core Loss Analysis of Permanent Magnet Linear Synchronous Generator Considering the 3-D Flux Path. *IEEE Trans. Magn.* **2018**, *54*, 8200604. [CrossRef]
20. Li, L.; Li, W.; Li, D.; Zhang, X.; Fan, Y. Influence of sleeve thickness and various structures on eddy current losses of rotor parts and temperature field in surface mounted permanent-magnet synchronous motor. *IET Electr. Power Appl.* **2018**, *12*, 1183–1191. [CrossRef]
21. Han, J.; Ge, B.; Li, W. Influence of Magnetic Permeability of the Press Plate on the Loss and Temperature of the End Part in the End Region of a Turbogenerator. *IEEE Trans. Ind. Electron.* **2019**, *66*, 162–171. [CrossRef]
22. Belahcen, A.; Arkkio, A. Computation of Additional Losses Due to Rotor Eccentricity in Electrical Machines. *IET Electr. Power Appl.* **2010**, *4*, 259–266. [CrossRef]
23. Kifune, H.; Zadhe, M.K.; Sasaki, H. Efficiency Estimation of Synchronous Generators for Marine Applications and Verification with Shop Trial Data and Real Ship Operation Data. *IEEE Access* **2020**, *8*, 195541–195550. [CrossRef]
24. Lu, B.; Habetler, T.G.; Harley, R.G. A Nonintrusive and In-Service Motor-Efficiency Estimation Method Using Air-Gap Torque with Considerations of Condition Monitoring. *IEEE Trans. Ind. Appl.* **2008**, *44*, 1666–1674. [CrossRef]
25. Gokasan, M.; Bogosyan, S.; Goering, D.J. Sliding Mode Based Powertrain Control for Efficiency Improvement in Series Hybrid-Electric Vehicles. *IEEE Trans. Power Electron.* **2006**, *21*, 779–790. [CrossRef]
26. Mirahki, H.; Moallem, M.; Rahimi, S.A. Design Optimization of IPMSM for 42 V Integrated Starter Alternator Using Lumped Parameter Model and Genetic Algorithms. *IEEE Trans. Magn.* **2014**, *50*, 114–119. [CrossRef]

27. Urase, K.; Yabu, N.; Kiyota, K.; Sugimoto, H.; Chiba, A.; Takemoto, M.; Ogasawara, S.; Hoshi, N. Energy Efficiency of SR and IPM Generators for Hybrid Electric Vehicle. *IEEE Trans. Ind. Appl.* **2015**, *51*, 2874–2883. [CrossRef]
28. Al-Adsani, A.S.; Beik, O. Design of a Multiphase Hybrid Permanent Magnet Generator for Series Hybrid EV. *IEEE Trans. Energy Convers.* **2018**, *33*, 1499–1507. [CrossRef]
29. Liu, Y.; Zhang, Y.; Xu, W.; Zhang, M.; Pan, W.; Rodriguez, J.; Boldea, I. Improved Efficiency Optimization Control for Brushless Doubly Fed Induction Generator–DC System by Regulating Stator Frequency. *IEEE Trans. Power Electron.* **2023**, *38*, 3624–3639. [CrossRef]
30. Grachev, P.Y.; Tabachinskiy, A.S.; Kanagavel, P. New Stator Construction and Simulation of High-Efficiency Wind Turbine Generators. *IEEE Trans. Ind. Appl.* **2020**, *56*, 1389–1396. [CrossRef]
31. Bonthu, S.S.R.; Choi, S.; Baek, J. Design Optimization with Multiphysics Analysis on External Rotor Permanent Magnet-Assisted Synchronous Reluctance Motors. *IEEE Trans. Energy Convers.* **2018**, *33*, 290–298. [CrossRef]
32. Wan, S.T.; He, Y.L.; Tang, G.J.; Li, Y.G. Analysis on Stator Circulating Current Characteristics under Eccentricity Faults of Turbo-Generator. *High Volt. Eng.* **2010**, *36*, 1547–1553.
33. Gao, J.; Dai, L.; Zhang, W.; Huang, S.; Wu, X. Multi-Interval Efficiency Design Optimization for Permanent Magnet Synchronous Generators Used in Hybrid Electric Special Vehicles. *IEEE Trans. Ind. Electron.* **2021**, *68*, 4646–4656. [CrossRef]
34. Zarko, D. A Systematic Approach to Optimized Design of Permanent Magnet Motors with Reduced Torque Pulsations. Ph.D. Thesis, The University of Wisconsin—Madison, Madison, WI, USA, 2004.
35. Ristanovic, D.; Taher, M.; Bhatia, N. Turbo-Expander Generators for Supplemental Power Generation in LNG Liquefaction Plants. *IEEE Trans. Ind. Appl.* **2020**, *56*, 6094–6103. [CrossRef]